This is a preprint, the final version is subject to change, of the American Mineralogist (MSA)
Cite as Authors (Year) Title. American Mineralogist, in press.
DOI: https://doi.org/10.2138/am-2018-6299

Revision 1

Melting experiments on Fe–Si–S alloys to core pressures: Silicon in the core?

SHIGEHIKO TATENO[1,*], KEI HIROSE[1,2], RYOSUKE SINMYO[1,2], GUILLAUME MORARD[3], NAOHISA HIRAO[4], AND YASUO OHISHI[4]

[1]Earth-Life Science Institute, Tokyo Institute of Technology, 2-12-1 Ookayama, Meguro, Tokyo 152-8550, Japan

[2]Department of Earth and Planetary Science, The University of Tokyo, 7-3-1 Hongo, Bunkyo, Tokyo 113-0033, Japan

[3]Institut de Minéralogie, de Physique des Matériaux et de Cosmochimie, UMR CNRS 7590, Sorbonne Universités – Université Pierre et Marie Curie, CNRS, Muséum National d'Histoire Naturelle, IRD, 4 Place Jussieu, 75005 Paris, France

[4]Japan Synchrotron Radiation Research Institute, 1-1-1 Kouto, Sayo-cho, Hyogo 679-5198, Japan

* E-mail: tateno@elsi.jp (S. Tateno)

ABSTRACT

Melting and subsolidus experiments were carried out on Fe–Si–S alloys (2.2–2.7 wt% Si + 2.0–2.1 wt% S) up to 146 GPa in a laser-heated diamond-anvil cell (DAC). The melting and subsolidus phase relations were examined on the basis of in-situ synchrotron X-ray diffraction measurements and ex-situ textural and chemical characterizations of recovered samples. The subsolidus phase assemblage changed from Fe-rich hexagonal closed-packed (hcp) phase + Fe_3S into a single phase of hcp Fe–Si–S alloy above 80 GPa at ~2500 K. The melting curve was obtained on the basis of the appearance of diffuse X-ray scattering and/or melting texture found in the cross section of a recovered sample. Microprobe analyses of quenched molten samples showed that liquid Fe–Si–S coexisted with Fe-alloy solid being depleted in sulfur but enriched in silicon compared to the liquid. This indicates that the liquid evolves toward a Si-poor and S-rich composition upon crystallization. Our data further suggest that the ternary eutectic liquid composition is Si-deficient and close to the tie line between the eutectic points in the Fe–Si and Fe–S binary systems at each pressure. The composition of Fe–Si–S liquid that accounts for the outer core density is outside the liquidus field of solid Fe at the inner core boundary (ICB) pressure. Accordingly, the solid alloy crystallizing from such outer core liquid must be more enriched in silicon/sulfur than the coexisting liquid and thus cannot form the denser inner core required from seismic observations. Furthermore, liquid Fe–Si–C nor Fe–Si–O does not crystallize a denser solid at the ICB. These reinforce the conclusion that silicon is not an important light element in the core.

Keywords: Core, light element, silicon, sulfur, high pressure, melting

42

43 ## INTRODUCTION

44 Sulfur has been studied as a possible light element in the core most extensively in
45 the past (see Figure 1 in Hirose et al. 2013). Earlier experimental works on the Fe–S
46 binary system showed that the eutectic composition moves toward the Fe-rich side with
47 increasing pressure (Brett and Bell, 1969; Stewart et al. 2007; Morard et al. 2008a;
48 Kamada et al. 2012). The most recent work by Mori et al. (2017) reported the eutectic
49 liquid with ~6 wt% S at 254 GPa, less than required (9–14 wt% S) to account for the
50 core density deficit (Sata et al. 2010; Huang et al. 2013; Badro et al. 2014; Umemoto et
51 al. 2014), suggesting that sulfur cannot be a single light component because otherwise
52 the less dense, S-rich CsCl (B2)-type phase crystallizes. Similarly silicon has been also
53 repeatedly proposed to be present in the core, although its concentration in the inner
54 core deduced from comparison between global seismic observations and high-pressure
55 mineral physics experiments ranges from 1–2 wt% Si (Antonangeli et al. 2010) to 4.5–8
56 wt% Si as a major light element (Fischer et al. 2014; Tateno et al. 2015). Recent
57 experiments demonstrated that the eutectic liquid in the Fe–Si binary includes only <2
58 wt% Si under core pressures (Ozawa et al. 2016), which is again less than the 6–12 wt%
59 Si that explains the outer core density deficit (Sata et al. 2010; Badro et al. 2014). It
60 excludes the possibility that silicon is a single light element in the core.
61 While both the Fe–S and Fe–Si binary systems have been investigated extensively
62 under high pressures (e.g., Fei et al. 2000; Morard et al. 2011; Fischer et al. 2013), little

is known about the Fe–Si–S ternary system (Sanloup and Fei 2004; Morard et al. 2008b; Sakairi et al. 2017). The liquid density measurements by Morard et al. (2013) proposed the outer core with 2 wt% Si and 6 wt% S. It is important to investigate phase equilibria in ternary systems, which can be very different from those of binary systems; for example, the Fe–Si–O ternary system exhibits very large liquidus field of SiO_2 oxide, leading to SiO_2 crystallization from liquid Fe–Si–O (>2 wt% Si + >2 wt% O) prior to Fe or Fe–Si metals (Hirose et al. 2017). In this study, we performed melting and subsolidus experiments on Fe–Si–S alloys and found that the partitioning of silicon between coexisting liquid and solid is different from that observed in the Fe–Si binary. We discuss that the outer core is not liquid Fe–Si–S because liquid iron including silicon and sulfur high enough to explain the core density deficit is outside the liquidus field of Fe at 330 GPa. Fe–Si–C and Fe–Si–O are also not likely. These suggest that silicon is not an important light element in the core.

EXPERIMENTAL METHODS

High-pressure and -temperature (*P*-*T*) conditions were generated using laser-heated DAC techniques (Table 1). Beveled 120 μm or flat 300 μm culet diamond anvils were used, depending on a target pressure. The Fe–Si–S starting materials were prepared by an ultra-rapid quench method described in Morard et al. (2011) and Mori et al. (2017). Chemical analyses using a field-emission-type electron probe microanalyzer (FE-EPMA, *JEOL* JXA-8530F) showed that they contain 2.2–2.7 wt% Si and 2.0–2.1 wt% S with 0.2–0.4 wt% O (Table 2). The sample was pressed into a thin foil with a

thickness of 10–20 μm and placed into a hole drilled in a rhenium gasket with thermal insulation layers of Al_2O_3 powder. After sample loading, a whole DAC was dried in a vacuum oven at 423 K, at least for 1 hr and then flushed with argon gas when the oven was opened. Subsequently the sample was compressed to high pressure in an argon atmosphere in a glove box. Heating was conducted at the BL10XU of SPring-8 or the Tokyo Tech, whose laser-heating systems are very similar to each other. The experiments at the former were combined with in-situ X-ray diffraction (XRD) measurements (Fig. 1a). Samples were heated from both sides with a couple of 100 W single-mode Yb fiber lasers (*SPI* or *IPG*). In order to reduce a radial temperature gradient, we employed beam shapers (*New focus*) that convert a beam with a Gaussian intensity distribution to the one with a flat-top distribution. The laser-heated spot was approximately 20 μm across. Heating duration in the present experiments was limited to 3 to 25 sec. The time-series experiments at 120–127 GPa by Ozawa et al. (2016) on the melting of Fe–Si alloy demonstrated that the result obtained with heating for 1 sec was well reproduced by that with heating for 5 sec. Similarly the data obtained by Mori et al. (2017) for melting an Fe–S alloy at 46 GPa by heating for 1 sec was very similar to that found by heating for 120 sec. These indicate that the present heating duration was long enough for the attainment of chemical equilibrium because the length scale is very short for a DAC sample.

Temperature was measured by a spectro-radiometric method (Ohishi et al. 2008). For experiments with in-situ XRD measurements (runs #1–5, 10, 11), its uncertainty corresponds to the temporal and spatial variations in 6 μm area from which XRD data

were collected. For runs in which we examined the cross section of recovered samples (runs #6–9), Table 1 shows both 1) the peak temperature in a measured radial profile, and 2) the temperature at the liquid/solid boundary that corresponds to a crystallization temperature. The latter was obtained by combining the temperature profile with a texture of sample cross section (Fig. 1b) (Ozawa et al. 2016; Hirose et al. 2017). The liquid/solid boundary should have been isothermal, and the sample cross sections given in Figure 1 show that temperature gradient was not so strong along the heating (compression) axis. The estimate of temperature at the liquid/solid boundary may include ±5 % error, except in run #7–2 in which the gradient was relatively large.

Pressures were measured after heating at 300 K, based on the unit-cell volume of Al_2O_3 corundum in runs #1–4 and #10–11 (Dewaele and Torrent 2013) or post-perovskite phase in run #5 (Ono et al. 2006) and by the Raman shift of the culet of a diamond anvil for runs #6–9 (Akahama and Kawamura 2006) (Table 1). The pressures measured after heating were similar between those calculated from corundum and from the Raman shift of a diamond anvil. Assuming thermal parameters same as those for pure iron (Dewaele et al. 2006), a pressure increase upon heating was found to be 5.4(±0.1) % per 1000 K for hcp Fe–Si–S in runs #3 and #5, which was applied to calculate thermal pressure contribution in all runs. The uncertainty in the present pressure determination may be ±10%.

Angle-dispersive XRD measurements were conducted at BL10XU, SPring-8 using an X-ray beam with an energy of ~30 keV (Ohishi et al. 2008). XRD patterns were collected on a flat panel detector (*Perkin Elmer*) sequentially during heating with an

exposure time of 1 sec. A monochromatic X-ray beam was focused and collimated to approximately 6 μm area (full-width of half maximum) on a sample position. Two-dimensional XRD image was integrated over the Debye–Scherrer rings using the IP Analyzer program (Seto et al. 2010), in order to produce a conventional one-dimensional diffraction pattern as a function of two-theta angle.

Textural and chemical characterizations were carried out for samples recovered from a DAC. A cross section of an exact laser-heated portion of a sample was prepared parallel to a compression axis by an argon ion-milling technique using an Ion Slicer (*JEOL* EM-09100 IS) (Tateno et al. 2009) or by a focused Ga ion beam (FIB) (*FEI* Versa^{TM} 3D DualBeam^{TM}). The sample cross section was then examined by a scanning electron microscope (FE-SEM) and an energy dispersive X-ray spectrometry (EDS) in the dual beam FIB system. For melting experiments, quantitative chemical analyses of coexisting quenched liquid and solid were obtained by FE-EPMA with an acceleration voltage of 10 kV and a beam current of 10 nA, except in run #7 in which EDS analyses were employed (accelerating voltage of 15 kV) (Table 2).

RESULTS

Subsolidus phase relation

We first examined the subsolidus phase relation of Fe–2.7wt%Si–2.1wt%S alloy in runs #1–5. In run #1, the sample was initially compressed to 41 GPa at room temperature, and broad diffraction peaks were observed from the hexagonal-close-packed (hcp) phase and a thermal insulator of corundum. The starting

sample consists of a mixture of Fe–Si and FeS. The former is observed to be an hcp phase under pressure. On the other hand, FeS was commonly found to become amorphous on compression (Ozawa et al. 2013; Mori et al. 2017). When it was heated to 1910 K at 43 GPa, the hcp diffractions became sharper and spotty, and additional reflections appeared, all of which are attributed to the tetragonal Fe_3S phase (Fei et al. 2000) (Fig. 2). Similar observation was obtained up to 67 GPa and 2310 K in run #2. On the other hand, in run #3, when heating the sample to 2670 K at 96 GPa, the spotty hcp peaks were solely observed without reflections from Fe_3S (Fig. 2). Hcp was confirmed as a single phase at 115–146 GPa and 2070–2470 K (runs #4 and #5) (Fig. 3a, Table 1).

These indicate that the solubility of sulfur in an hcp Fe–Si alloy is enhanced with increasing pressure, consistent with the observations for hcp Fe in the Fe–Fe_3S binary system (Kamada et al. 2012; Mori et al. 2017). The hcp Fe–2.7wt%Si can accommodate 2.1 wt% S above ~80 GPa (Fig. 3a), which is comparable to the solubility of sulfur in hcp iron, ~3 wt% at this pressure range, in the Fe–Fe_3S binary (Mori et al. 2017).

Melting temperature

The melting temperature of Fe–2.7wt%Si–2.1wt%S alloy was determined in-situ on the basis of a diffuse signal in XRD images (Fig. 1a). In run #6, the hcp phase was found, together with a thermal insulator of corundum, in the XRD pattern before heating. We increased the temperature of this sample from 300 K directly to 2550 K (at the hottest spot) at 52 GPa (Table 1). The XRD patterns collected sequentially every 1 sec

exhibited diffuse scattering from the onset of laser heating, the clear evidence for melting, together with the peaks from the face-centered cubic (fcc) phase. Such diffuse signal was preserved even after quenching temperature to 300 K. Similar observations were made at 20–28 GPa in runs #10–11.

In addition, the melting temperature was constrained by the temperature at the liquid/solid boundary in runs #6–9 without X-ray observations (Table 1). Indeed, the temperature at the boundary was found to be 2350 K in run #6, lower than the 2550 K at the hottest part. Thus, the temperature at the liquid/solid interface better constrains the melting temperature (Fig. 3a). The samples recovered from 96 GPa/2670 K (run #3) exhibited no evidence for melting under the FIB/SEM.

The solidus curve of Fe + 2.2–2.7wt%Si + 2.0–2.1wt%S is shown in Figures 3a and 3b, in comparison with those of pure Fe and alloys in the latter. The change in a subsolidus phase assemblage from hcp + Fe_3S into hcp single phase leads to a kink around 80 GPa. Our data show that the solidus in the present Fe + 2.2–2.7wt%Si + 2.0–2.1wt%S alloy is higher than that of the Fe–S binary because silicon is a compatible element that partitions more into solid than in liquid in the Fe–Si–S system (see the next section for liquid/solid partitioning). Similar effect was found for the incorporation of nickel into the Fe–S system (Stewart et al. 2007). The recent DAC experiment by Sakairi et al. (2017) also studied Fe–Si–S alloys (4 wt% Si + 8–12 wt% S) and reported a solidus curve 400 K lower than ours at 60 GPa. A main source of the discrepancy could be different melting diagnostics; while we employed 1) the presence/absence of diffuse X-ray signal and/or 2) melting texture in recovered samples as melting criteria,

Sakairi and others judged the onset of melting from the disappearance of reflection lines from one solid phase in an XRD pattern. Indeed, the disappearance of XRD peaks is not necessarily caused by melting in particular in angle-dispersive diffraction measurements. Instead, a rapid crystal growth before melting could lead to the disappearance of reflection lines within an observed 2-theta angle range, possibly providing apparent lower melting temperature than ours.

Melting texture and the compositions of coexisting liquid and solid

We examined the cross sections of quenched molten samples from runs #6–7 performed at ~50 GPa and runs #8–9 at ~130 GPa close to the pressure at CMB (Table 1, Fig. 3a). The sample recovered from run #6, in which a diffuse XRD signal characteristic of liquid was observed (Fig. 1a), exhibited a smooth and uniform area at the center of a laser-heated spot (Fig. 1b). This portion represents a quenched liquid, which is also evident from the entrainment of Al_2O_3 grains from a surrounding pressure medium. Furthermore, such smooth texture without any crystalline phase is consistent with the observed diffuse scattering halo preserved after quenching temperature. This is likely due to a fast quenching speed, which allows us to determine the melt composition correctly. Next to the liquid portion, we found a residual solid with a texture showing a channeling contrast (Fig. 1b), which is due to the different intensity in backscattered electron that reflects different crystal orientation. The boundary between coexisting liquid and solid was hourglass-shaped, in accordance with isothermal surface typical for a metallic sample (Campbell et al. 2007). Such melting texture is caused by a certain

temperature gradient (Lesher and Walker 1988) and similar to those observed in previous experiments on a variety of iron alloys (Ozawa et al. 2016; Mori et al. 2017; Hirose et al. 2017). The sample was molten also in runs #7–9; melt pockets became smaller with decreasing temperature at each pressure range (Fig. 1c). In all of these experiments conducted above 47 GPa, the liquid was homogeneous, consistent with the previous report by Sanloup and Fei (2004) that liquid miscibility gap closes above 15 GPa in the Fe–Si–S system.

The chemical compositions of coexisting liquid and residual solid in runs #6–9 and their proportions in wt% based on mass balance are given in Table 2 and plotted in the Fe–Si–S ternary diagram (Fig. 4a). Liquids are enriched in sulfur and depleted in silicon compared to the starting composition in all the experiments (Fig. 1c). Instead, residual solids right next to the liquid are depleted in sulfur and enriched in silicon.

The XRD observations in run #6 indicate that liquid Fe–1.2wt%Si–8.1wt%S coexisted with an fcc Fe-rich phase at 52 GPa. Considering the binary eutectic compositions at 50 GPa, Fe–8wt%Si in Fe–FeSi (Ozawa et al. 2016) and Fe–13wt%S in Fe–Fe_3S (Mori et al., 2017), the liquidus field of the fcc Fe-rich phase covers all of three liquid compositions (1.1–1.4 wt% Si and 8.1–11.2 wt% S) obtained in this pressure range (Fig. 4a). On the other hand, solids found at 128–129 GPa (runs #8–9) containing 2.5–2.8 wt% Si and 1.0–1.8 wt% S may be the CsCl (B2)-type phase, since silicon concentration in the Fe–FeSi eutectic liquid decreases with increasing pressure and is 1.5 wt% Si at ~130 GPa (Ozawa et al. 2016). It means that the coexisting liquid compositions (Fe + 0.7–1.6 wt% Si + 3.9–5.6 wt% S) are in the liquidus field of the

CsCl-type phase (Fig. 4a).

DISCUSSION

Evolution of liquid in the Fe–Si–S ternary

Present melting experiments in the Fe–Si–S ternary system demonstrate that solid is enriched in silicon and depleted in sulfur compared to coexisting liquid, leading to the evolution of liquid toward Si-poor and S-rich upon crystallization (Fig. 4a). This can be reasonably interpreted by the liquidus surface topology of iron (Fig. 4b). Simple linear interpolation between pure Fe and the eutectic liquids gives the depression of the liquidus temperatures to be -30 K/wt% by silicon and -100 K/wt% by sulfur according to Morard et al. (2014). The more recent experiments performed by Mori et al. (2017) reported about -160 K/wt% by sulfur addition at 130 GPa. Consequently, the liquidus surface (temperature) of Si-rich side within the Fe liquidus field is higher than that of the S-rich side, resulting in the liquid composition changing to Si-poor and S-rich along the liquidus surface followed temperature downward the eutectic point.

At 50 GPa, binary eutectic points are located at 8 wt% silicon and 2750 K in Fe–FeSi (Ozawa et al. 2016; Fischer et al. 2013) and at 13 wt% sulfur and 1900 K in Fe–Fe_3S, which are 250 K and 1100 K lower than the melting point of pure Fe (Anzellini et al. 2013), respectively. With decreasing temperature from 2350 to 2070 K in the present experiments (runs #6, #7-1, #7-2), sulfur concentration in liquid was enhanced from 8.1 to 11.2 wt%, while silicon abundance was nearly constant at ~1 wt% (Table 2). The liquid composition obtained at 2070 K is plotted near the tie line between the Fe–Si and

Fe–S binary eutectic compositions at this pressure range (Fig. 4a), suggesting that it is close to the Fe–Si–S ternary eutectic composition. Indeed, the proportion of this liquid is calculated to be as small as 9 wt%.

With increasing pressure to ~130 GPa (runs #8–9), nearly corresponding to the pressure of the topmost core, liquid compositions became poor in sulfur in accordance with the decrease in sulfur concentration in the Fe–S binary eutectic liquid (Mori et al. 2017). The coexisting solid phases included more silicon and less sulfur (2.5–2.8 wt% Si and 1.0–1.8 wt% S) than liquids (0.7–1.6 wt% Si and 3.9–5.6 wt% S) (Table 2). The crystallization of such solid evolves liquid into a Si-poor and S-rich composition upon cooling (Fig. 4a), consistent with the higher liquidus temperature in the Fe–Si side than in the Fe–S side as discussed above (Fig. 4b). The liquid obtained at 3410 K included 5.6 wt% S and 0.7 wt% Si, less sulfur and similar silicon contents than those found in a series of experiments at ~50 GPa. This liquid composition is again located near the tie line between the Fe–Si and Fe–S binary eutectic compositions at 130 GPa and might therefore be close to the ternary eutectic composition (Fig. 4a). The liquid **proportion** of this experiment was 8 wt%.

Fe–Si–S liquid in the core?

The silicon concentration in the eutectic liquid in the Fe–Si binary system decreases with increasing pressure (Ozawa et al. 2016) and is likely to be 1 wt% Si or less at 330 GPa. The recent experiments performed by Mori et al. (2017) also demonstrated that the eutectic liquid in the Fe–S binary becomes depleted in sulfur to 5.7 wt% with increasing

283 pressure to 254 GPa. The possible ternary eutectic point at 330 GPa is likely to be
284 S-rich and close to the tie line between the binary eutectic compositions (Fig. 4a),
285 considering those at 50 GPa and 130 GPa that were constrained in the present
286 experiments.

287 The density jump of ~4.5% across the ICB (Shearer and Masters 1990; Masters and
288 Gubbins 2003) is greater than the density change on melting of iron (~1%) (Brown and
289 McQueen 1986; Komabayashi and Fei 2010; Ichikawa et al. 2014), suggesting that the
290 solid inner core is depleted in light element compared to the liquid outer core. The static
291 compression experiments and *ab initio* calculations have argued that the density at the
292 outer core side of the ICB is explained by the presence of 6-12 wt% Si or 9-14 wt% S
293 assuming a sole light element in liquid iron (Sata et al. 2010; Badro et al. 2014;
294 Umemoto et al. 2014) (Fig. 5a). Similarly, the inner core composition was estimated to
295 be 4.2-6.0 wt% Si or 5.7-6.6 wt% S, which matches the observed density at the ICB
296 (Sata et al. 2010; Sakai et al. 2012; Tateno et al. 2015).

297 These previous estimates of a possible range of silicon and sulfur contents in the
298 liquid core are certainly more enriched in silicon/sulfur than the Fe–Si–S ternary
299 eutectic liquid at 330 GPa (Fig. 5a) and outside the liquidus field of iron. If this is the
300 case, a solid alloy crystallizing from such core liquid must be more enriched in Si/S
301 than the liquid and have CsCl (B2)-type crystal structure. Since the inner core solid
302 must be depleted in Si/S as shown in Figure 5a, our ternary phase diagram precludes the
303 presence of Fe–Si–S liquid in the outer core.

304

IMPLICATIONS

We also consider the possibility of other Fe–Si–X liquids in the outer core. The likely liquidus phase relations in the Fe–Si–C ternary system is illustrated in Figure 5b. Sata et al. (2010) estimated 9.2 wt% C in the outer core to explain the density deficit from pure iron at the ICB. The *ab initio* calculations by Badro et al. (2014) argued that 4.2 wt% C is required to account for the liquid core density at the ICB. The possible Fe–Si–C liquid in the outer core may be on the join between Fe + 6–12 wt% Si (as discussed above) and Fe + 4.2–9.2 wt% C. On the other hand, thermodynamic calculations have suggested that the eutectic liquid in the Fe–C binary becomes depleted in carbon with increasing pressure (Wood 1993) and may include only about 2 wt% C at 330 GPa (Fei and Brosh 2014). It is likely that the Fe–Si–C ternary eutectic point is located close to the tie line between the eutectic points in the Fe–Si and Fe–C systems as found in the Fe–Si–S ternary system in this study. Therefore, the possible Fe–Si–C liquid compositions are again outside the liquidus field of iron.

Regarding liquid Fe–Si–O, the simultaneous solubility of silicon and oxygen in molten iron is limited under the present-day core temperature. Hirose et al. (2017) argued that the current outer core has been subjected to SiO_2 crystallization and is now depleted in either Si (< 0.7 wt.%) or O (< 1.0 wt.%) if the CMB temperature is at 4000 K.

The *ab initio* calculations by Umemoto and Hirose (2015) demonstrated that the density and compressional velocity of liquid Fe + 1.0 wt% H match seismological observations. The eutectic liquid composition in the Fe–H binary is supposed to be

enriched in hydrogen more than FeH (Fe + 1.8 wt% H) at 15 GPa (Shibazaki et al. 2014). The multi-anvil experiments performed below 20 GPa by Sakamaki et al. (2009) reported that the melting temperature of FeH is substantially lower than those of Fe and other Fe alloys at that pressure range. The melting phase relations in Fe–H alloys have been proposed at ~100 GPa (Fukai 1992), and if they remain similar with increasing pressure to 330 GPa, a possible range of Fe–Si–H core liquid compositions are partly within the liquidus field of Fe (Fig. 5c). The hydrogen-rich Fe–Si–H liquids might be therefore compatible with the density jump across the ICB.

These suggest that the outer core is composed neither of Fe–Si–S, Fe–Si–C, nor Fe–Si–O ternary liquids. Although hydrogen-rich Fe–Si–H liquid is not excluded, it is likely that silicon is not an important light element in the core.

ACKNOWLEDGMENTS

This work was supported by JSPS research grant No. 24000005. XRD measurements were conducted at SPring-8 (proposal no. 2014B0087 and 2015A0087). Comments from D. Walker, an anonymous reviewer, and the Editor were helpful to improve the manuscript.

REFERENCE CITED

Akahama, Y., and Kawamura H. (2006) Pressure calibration of diamond anvil Raman gauge to 310 GPa. Journal of Applied Physics, 100, 043516.

Antonangeli, D., Siebert J., Badro, J., Farber D.L., Fiquet, G., Morard, G., and Ryerson, F.J. (2010) Composition of the Earth's inner core from high-pressure sound velocity measurements in Fe–Ni–Si alloys. Earth and Planetary Science Letters, 295, 292–296.

Anzellini, S., Dewaele, A., Mezouar, M., Loubeyre, P., and Morard, G. (2013) Melting of iron at Earth's inner core boundary based on fast X-ray diffraction. Science 340, 464–466.

Badro, J., Côté, A.S., and Brodholt, J.P. (2014) A seismologically consistent compositional model of Earth's core. Proceedings of the National Academy of Sciences, 111, 7542–7545.

Brett, R., and Bell, P.M. (1969) Melting relations in the Fe-rich portion of the system Fe–FeS at 30 kb pressure. Earth and Planetary Science Letters, 6, 479–482.

Brown, J. M., and R. G. McQueen (1986), Phase transitions, Grüneisen parameter, and elasticity for shocked iron between 77 GPa and 400 GPa, J. Geophys. Res., 91(B7), 7485–7494.

Campbell, A.J., Seagle, C.T., Heinz, D.L., Shen, G., and Prakapenka, V.B. (2007) Partial melting in the iron–sulfur system at high pressure: a synchrotron X-ray diffraction study. Physics of the Earth and Planetary Interiors, 162, 119–128.

Dewaele, A., Loubeyre, P., Occelli, F., Mezouar, M., Dorogokupets, P.I., and Torrent, M.

(2006) Quasihydrostatic equation of state of iron above 2 Mbar. Physical Review Letters, 97, 215504.

Dewaele, A., and Torrent M. (2013) Equation of state of α-Al_2O_3. Physical Review Letters B, 88, 064107.

Fei, Y., and Brosh, E. (2014) Experimental study and thermodynamic calculations of phase relations in the Fe–C system at high pressure. Earth and Planetary Science Letters, 408, 155–162.

Fei, Y., Li, J., Bertka, C.M., and Prewitt, C.T. (2000) Structure type and bulk modulus of Fe_3S, a new iron–sulfur compound. American Mineralogist, 85, 1830–1833.

Fischer, R.A., Campbell, A.J., Reaman, D.M., Miller, N.A., Heinz, D.L., Dera, P., and Prakapenka, V.B. (2013) Phase relations in the Fe–FeSi system at high pressures and temperatures. Earth and Planetary Science Letters, 373, 54–64.

Fischer, R.A., Campbell, A.J., Caracas, R., Reaman, D.M., Heinz, D.L., Dera, P., and Prakapenka, V.B. (2014) Equations of state in the Fe–FeSi system at high pressures and temperatures. Journal of Geophysical Research, 119, 2810–2827.

Fukai, Y. (1992) Some properties of the Fe–H system at high-pressure and temperatures, and their implications for the Earth's core. In: Syono, Y., and Manghnani, M.H. (Eds.), High-Pressure Research: Application to Earth and Planetary Sciences, American Geophysical Union, Geophysics Monograph Series, 67, pp. 373–386.

Hirose, K., Labrosse, S., and Hernlund, J. (2013) Composition and state of the core. Annual Review of Earth and Planetary Sciences, 41, 657–691.

Hirose, K., Morard, G., Sinmyo, R., Umemoto, K., Hernlund, J., Helffrich, G., and

Labrosse, S. (2017) Crystallization of silicon dioxide and compositional evolution of the Earth's core. Nature, 543, 99–102.

Huang, H., Wu, S., Hu, X., Wang, Q., Wang, X., and Fei, Y. (2013) Shock compression of Fe–FeS mixture up to 204 GPa. Geophysical Research Letters, 40, 687–691.

Kamada, S., Ohtani, E., Terasaki, H., Sakai, T., Miyahara, M., Ohishi, Y., and Hirao, N. (2012) Melting relationships in the Fe–Fe_3S system up to the outer core conditions. Earth and Planetary Science Letters, 359, 26–33.

Komabayashi, T., and Fei, Y. (2010) Internally consistent thermodynamic database for iron to the Earth's core conditions. Journal of Geophysical Research Solid Earth, 115, B03202.

Ichikawa, H., Tsuchiya, T., and Tange, Y. (2014) The P-V-T equation of state and thermodynamic properties of liquid iron. 2017/12/12 20, 119, B010732.

Lesher, C.E., and Walker, D. (1988) Cumulate maturation and melt migration in a temperature gradient. Journal of Geophysical Research Solid Earth, 93, 10295–10311.

Liu, J., Lin, J-F., Alatas, A., Hu, M.Y., Zhao, J., and Dubrovinsky, L. (2016) Seismic parameters of hcp-Fe alloyed with Ni and Si in the Earth's inner core. Journal of Geophysical Research Solid Earth, 121, 610–623.

Masters, T.G., and Gubbins, D. (2003) On the resolution of density within the Earth. Physics of the Earth and Planetary Interiors, 140, 159–167.

Morard, G., Andrault, D., Guignot, N., Sanloup, C., Mezouar, M., Petitgirard, S., and Fiquet, G. (2008a) In situ determination of Fe–Fe_3S phase diagram and liquid

411 structural properties up to 65 GPa. Earth and Planetary Science Letters, 272, 620–
412 626.
413 Morard, G., Sanloup, C., Guillot, B., Fiquet, G., Mezouar, M., Perrillat, J. P., Garbarino,
414 G., Mibe, K., Komabayashi, T., and Funakoshi, K. (2008b) In situ structural
415 investigation of Fe–S–Si immiscible liquid system and evolution of Fe–S bond
416 properties with pressure. Journal of Geophysical Research, 113, B10205.
417 Morard, G., Andrault, D., Guignot, N., Siebert, J., Garbarino, G., and Antonangeli, D.
418 (2011) Melting of Fe–Ni–Si and Fe–Ni–S alloys at megabar pressures:
419 implications for the core–mantle boundary temperature. Physics and Chemistry of
420 Minerals, 38, 767–776.
421 Morard, G., Siebert, J., Andrault, D., Guignot, N., Garbarino, G., Guyot, F., and
422 Antonangeli, D. (2013) The Earth's core composition from high pressure density
423 measurements of liquid iron alloys. Earth and Planetary Science Letters, 373, 169–
424 178.
425 Morard, G., Andrault, D., Antonangeli, D., and Bouchet, J. (2014) Properties of iron
426 alloys under the Earth's core conditions, Comptes Rendus Geoscience. 346, 130–
427 139.
428 Mori, Y., Ozawa, H., Hirose, K., Sinmyo, R., Tateno, S., Morard, G., and Ohishi Y.
429 (2017) Melting experiments on Fe–Fe_3S system to 254 GPa. Earth and Planetary
430 Science Letters, 464, 135–141.
431 Ohishi, Y., Hirao, N., Sata, N., Hirose, K., and Takata, M. (2008) Highly intense
432 monochromatic X-ray diffraction facility for high-pressure research at SPring-8.

High Pressure Research, 28, 163–173.

Ono, S., Oganov, A.R., Koyama, T., and Shimizu, H. (2006) Stability and compressibility of the high-pressure phases of Al_2O_3 up to 200 GPa: implications for the electrical conductivity of the base of the lower mantle. Earth and Planetary Science Letters, 246, 326–335.

Ozawa, H., Hirose, K., Suzuki, T., Ohishi, Y., and Hirao, N. (2013) Decomposition of Fe_3S above 250 GPa. Geophysical Research Letters, 40, 4845–4849.

Ozawa, H., Hirose, K., Yonemitsu, K., and Ohishi, Y. (2016) High-pressure melting experiments on Fe–Si alloys and implications for silicon as a light element in the core. Earth and Planetary Science Letters, 456, 47–54.

Sakai, T., Ohtani, E., Kamada, S., Terasaki, H., and Hirao, N. (2012) Compression of $Fe_{88.1}Ni_{9.1}S_{2.8}$ alloy up to the pressure of Earth's inner core. Journal of Geophysical Research Solid Earth, 117, B02210.

Sakairi, T., Ohtani, E., Kamada, S., Sakai, T., Sakamaki, T., and Hirao, N. (2017) Melting relations in the Fe–S–Si system at high pressure and temperature: implications for the planetary core. Progress in Earth and Planetary Science, 4, 10.

Sakamaki, K., Takahashi, E., Nakajima, N., Nishihara, Y., Funakoshi, K., Suzuki, T., and Fukai, Y. (2009) Melting phase relation of FeHx up to 20 GPa: implication for the temperature of the Earth's core. Physics of the Earth and Planetary Interiors, 174, 192–201.

Sanloup C., and Fei Y. (2004) Closure of the Fe–S–Si liquid miscibility gap at high

pressure. Physics of the Earth and Planetary Interiors, 147, 57–65.

Sata, N., Hirose, K., Shen, G., Nakajima, Y., Ohishi, Y., Hirao, N. (2010) Compression of FeSi, Fe_3C, $Fe_{0.95}O$, and FeS under the core pressures and implication for light element in the Earth's core. Journal of Geophysical Research Solid Earth, 115, B09204.

Seto, Y., Nishio-Hamane, D., Nagai, T., Sata, N. (2010) Development of a software suite on X-ray diffraction experiments. The Review of High Pressure Science and Technology, 20, 269–276.

Shearer, P.M. and Masters, T.G. (1990) The density and shear velocity contrast at the inner core boundary, Geophysical Journal International, 102, 491–498.

Shibazaki, Y., Terasaki, H., Ohtani, E., Tateyama, R., Nishida, K., Funakoshi, K., and Higo, Y. (2014) High-pressure and high-temperature phase diagram for $Fe_{0.9}Ni_{0.1}$–H alloy. Physics of the Earth and Planetary Interiors, 228, 192–201.

Stewart, A.J., Schmidt, M.W., van Westrenen, W., and Liebske, C. (2007) Mars: a new core–crystallization regime. Science, 316, 1323–1325.

Tateno, S., Sinmyo, R., Hirose, K., and Nishioka, H. (2009) The advanced ion-milling method for preparation of thin film using Ion Slicer: application to a sample recovered from diamond-anvil cell. Review of Scientific Instruments, 80, 013901.

Tateno, S., Kuwayama, Y., Hirose, K., and Ohishi, Y. (2015) The structure of Fe–Si alloy in Earth's inner core. Earth and Planetary Science Letters, 418, 11–19.

Umemoto, K., and Hirose, K. (2015) Liquid iron-hydrogen alloys at outer core conditions by first-principles calculations. Geophysical Research

Letters, 42, 7513–7520.

Umemoto, K., Hirose, K., Imada, S., Nakajima, Y., Komabayashi, T., Tsutsui, S., and Baron, A.Q.R. (2014) Liquid iron–sulfur alloys at outer core conditions by first-principles calculations. Geophysical Research Letters, 41, 6712–6717.

Wood, B.J. (1993) Carbon in the core? Earth and Planetary Science Letters, 117, 593–607.

Figure captions

FIGURE. 1. (a) Two-dimensional XRD image in run #6 collected before heating, during heating, and after quenching temperature. Melting of a sample was evident from diffuse scattering halo coexisting with fcc Fe. (b) (upper) Back-scattered electron image of the sample recovered from run #6 same as (a). A homogeneous liquid at the center coexisted with solid showing a clear channeling contrast. (lower) Corresponding temperature profile at the surface of the sample, showing the temperature at the liquid/solid boundary was 2350 K. (c) X-ray maps showing the sulfur and silicon concentrations in the sample recovered from run #7–2.

FIGURE. 2. XRD patterns showing the coexistence of hcp Fe and Fe_3S (S) at 43 GPa (lower panel) and the hcp single-phase at 96 GPa. C, Al_2O_3 corundum (thermal insulator); Re, rhenium (gasket).

FIGURE. 3. (a) Phase diagram of Fe–Si–S alloy (2.2–2.7 wt% Si + 2.0–2.1 wt% S). Inverse triangles, above solidus (closed symbols, melting confirmed by texture); triangles, subsolidus. Melting curve of Fe + 4 wt% Si + 8–12 wt% S is also shown (Sakairi et al. 2017). (b) Eutectic melting curves for Fe–9wt%Si (Fischer et al., 2013), pure Fe (Anzellini et al. 2013), Fe–5wt%Ni–15wt%Si (Morard et al. 2011), and the Fe–Fe_3S binary system (Mori et al. 2017) compared with that of the Fe–Si–S alloy given in (a).

FIGURE. 4. (a) Liquidus phase relations in the Fe–Si–S ternary system at 50 GPa (purple), 130 GPa (green), and 330 GPa (red). Coexisting liquid and solid compositions obtained in the present experiments are shown by filled and open triangles, respectively. Solid circles denote the binary eutectic compositions in the Fe–FeSi (Ozawa et al. 2016) and Fe–Fe_3S systems (Mori et al. 2017). (b) Topology of the liquidus surface in the Fe–FeSi–Fe_3S ternary system. Note the higher liquidus temperature for a Si-rich composition.

FIGURE. 5.

Possible liquidus phase relations in the Fe–Si–X ternary systems at 330 GPa. A gray region shows a likely range for the outer and inner core compositions that explains the seismically deduced density at the ICB (see text for details). Red circles indicate the eutectic liquid compositions in the binary system, which are taken from the literatures (Fei and Brosh, 2014; Shibazaki et al. 2014; Ozawa et al. 2016; Mori et al. 2017. The Fe–Si–H outer core liquid might evolve toward a silicon/hydrogen-rich composition by crystallizing iron-rich solid at the inner core.

This is a preprint, the final version is subject to change, of the American Mineralogist (MSA)
Cite as Authors (Year) Title. American Mineralogist, in press.
DOI: https://doi.org/10.2138/am-2018-6299

TABLE 1. Experimental conditions and phases observed.

run #	Pressure (GPa)			Temperature (K)		Duration (sec)	Obser
	after heating		on heating	Peak	Liq/sol boundary		in situ
	Al_2O_3	Raman					
Subsolidus experiment							
1	40	41	43 (4)	1910 (80)		25	hcp + Fe_3S
2	60	n.m.	67 (7)	2310 (100)		15	hcp + Fe_3S
3	85	83	96 (10)	2670 (110)		15	hcp
4	103	n.m.	115 (12)	2470 (150)		20	hcp
5	133	n.m.	146 (15)	2070 (170)		20	hcp
Melting experiment							
6	50	47	52 (5)	2550 (50)	2350 (120)	20	fcc + liquid
7-1		43	47 (5)	2250	2150 (120)	5	
7-2		43	47 (5)	2320	2070 (160)	5	
8		110	128 (13)	3630	3410 (170)	3	
9		110	129 (13)	4510	3570 (180)	3	
10	18	24	20 (2)	1750 (180)		15	fcc + liquid
11	25	24	28 (3)	2440 (170)		25	fcc + liquid

Note: Number in parentheses denote uncertainty in the last digit. n.m.; not measured

This is a preprint, the final version is subject to change, of the American Mineralogist (MSA)
Cite as Authors (Year) Title. American Mineralogist, in press.
DOI: https://doi.org/10.2138/am-2018-6299

vation
ex situ

solid +liquid
solid +liquid
solid +liquid
solid +liquid
solid +liquid

This is a preprint, the final version is subject to change, of the American Mineralogist (MSA)
Cite as Authors (Year) Title. American Mineralogist, in press.
DOI: https://doi.org/10.2138/am-2018-6299

TABLE 2. Chemical compositions of quenched liquid and coexisting solid (wt%).

Run#	Starting material-1	#6		#7-1		#7-2	
P (GPa)		52		47		47	
T (K)[a]		2350		2150		2070	
	EPMA	*EPMA*		*EDS*		*EDS*	
		Liquid	Solid	Liquid	Solid	Liquid	Solid
Fe	92.5 (0.5)	84.6 (0.4)	91.5 (0.5)	89.6 (0.1)	95.9 (0.3)	87.4 (0.2)	95.4 (0.2)
Si	2.7 (0.1)	1.2 (0.1)	3.3 (0.1)	1.1 (0.1)	3.1 (0.3)	1.4 (0.1)	3.4 (0.3)
S	2.1 (0.2)	8.1 (0.2)	1.0 (0.1)	9.3 (0.2)	1.0 (0.1)	11.2 (0.2)	1.3 (0.1)
O	0.4 (0.1)						
Total	97.7 (0.6)	93.9 (0.4)	95.8 (0.5)	100	100	100	100
Proportion[c]		17	83	14	86	9	91

Note: Numbers in parentheses indicate 1σ (2σ for Starting material-1) uncertainties of multiple measu

[a] Temperatures at the liquid/solid boundary.

[b] EPMA analyses of liquid and residual solid were contaminated by pressure medium and normalized

[c] Phase proportions (wt%) were calculated by mass balance.

Starting material-2	#8[b]		#9	
	128		129	
	3410		3570	
EPMA	*EPMA*		*EPMA*	
	Liquid	Solid	Liquid	Solid
91.7 (0.5)	93.8 (0.1)	95.7 (0.1)	94.1 (0.1)	94.3 (1.8)
2.2 (0.1)	0.7 (0.2)	2.5 (0.1)	1.6 (0.0)	2.8 (0.2)
2.0 (0.1)	5.6 (0.2)	1.8 (0.1)	3.9 (0.1)	1.0 (0.1)
0.2 (0.0)				
96.1	100	100	99.9	98.4
	8	92	35	65

ırements for liquid/solid and starting materials.

to 100% without Al and O.

This is a preprint, the final version is subject to change, of the American Mineralogist (MSA)
Cite as Authors (Year) Title. American Mineralogist, in press.
DOI: https://doi.org/10.2138/am-2018-6299

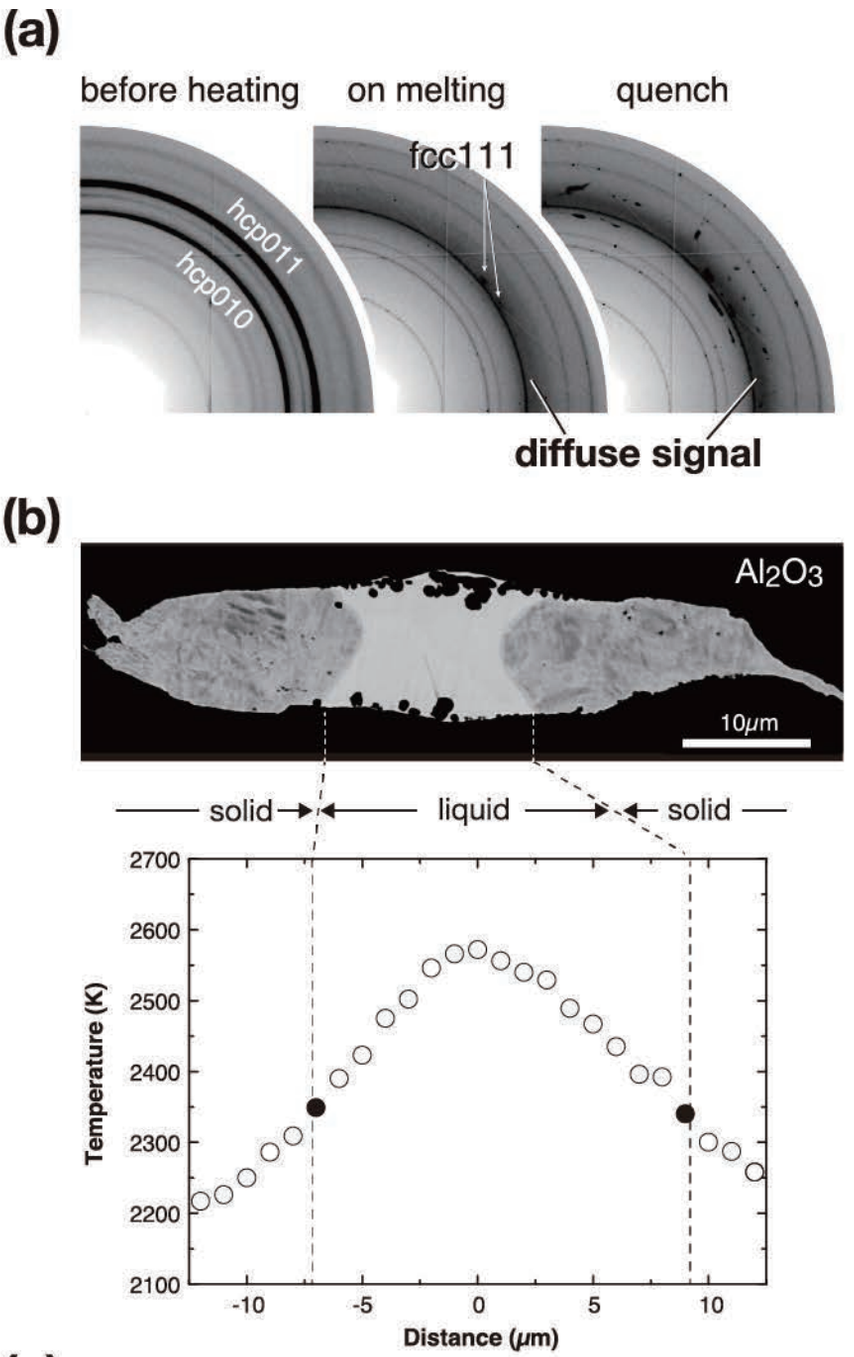

Fig. 1

This is a preprint, the final version is subject to change, of the American Mineralogist (MSA)
Cite as Authors (Year) Title. American Mineralogist, in press.
DOI: https://doi.org/10.2138/am-2018-6299

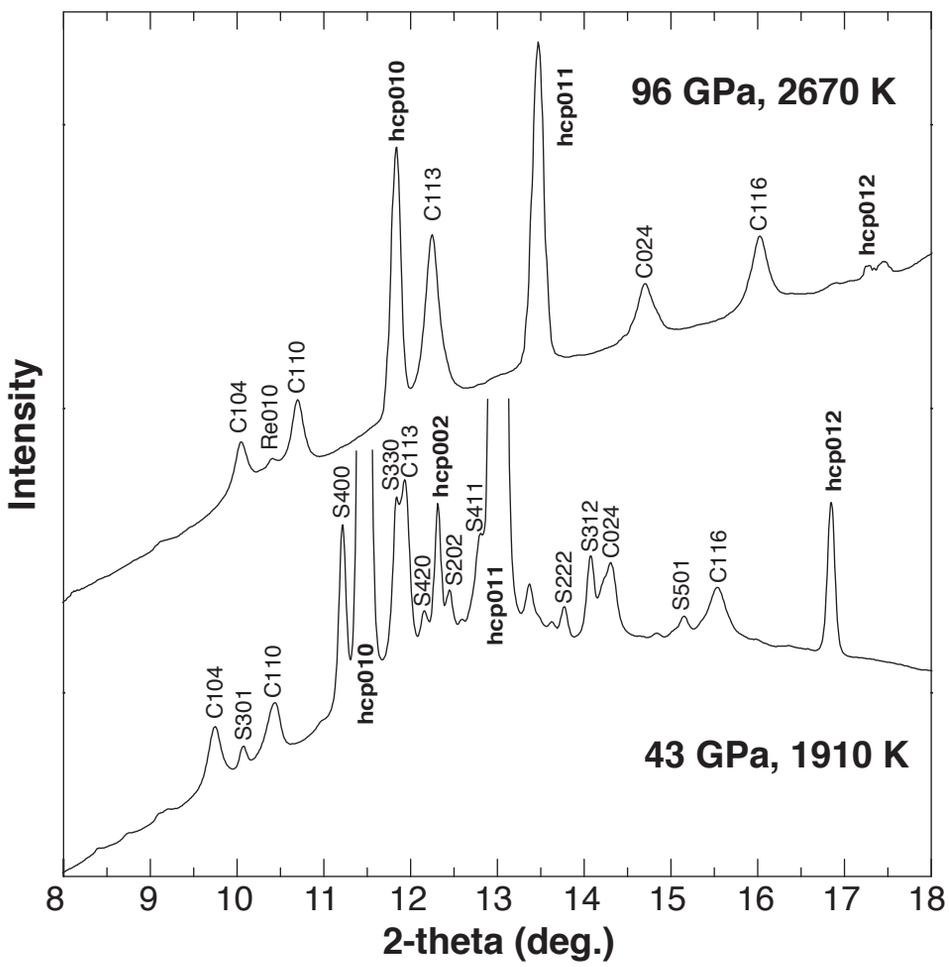

Fig. 2

This is a preprint, the final version is subject to change, of the American Mineralogist (MSA)
Cite as Authors (Year) Title. American Mineralogist, in press.
DOI: https://doi.org/10.2138/am-2018-6299

(a)

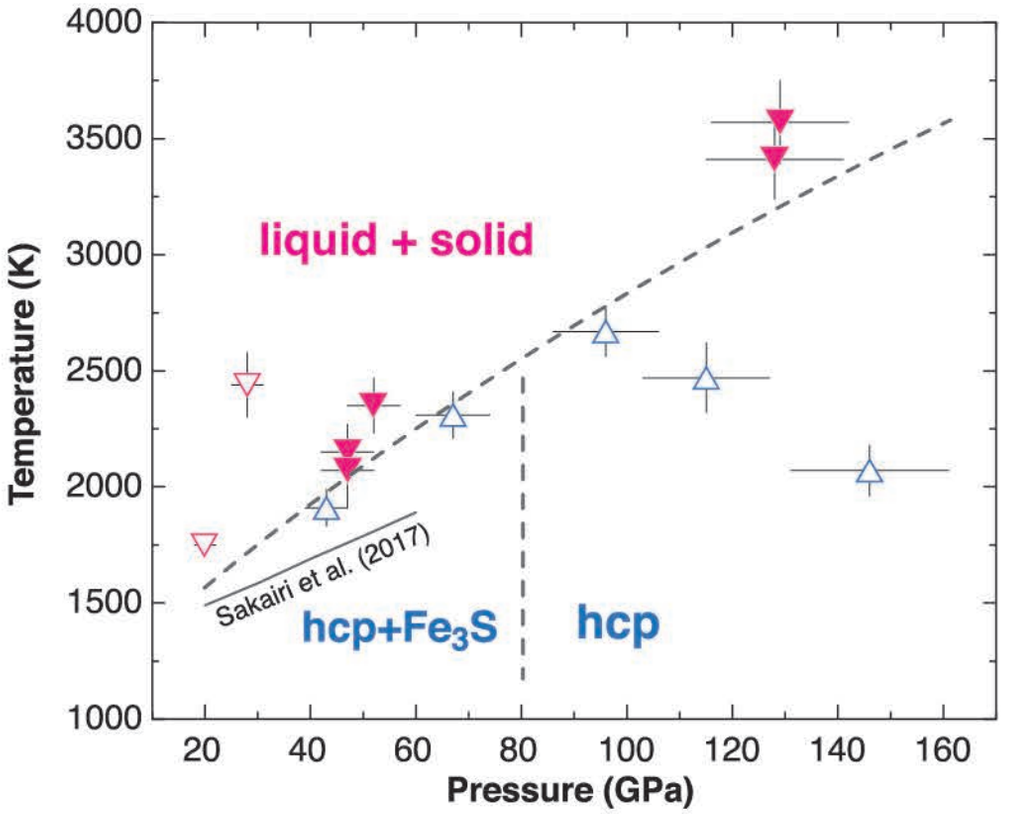

(b)

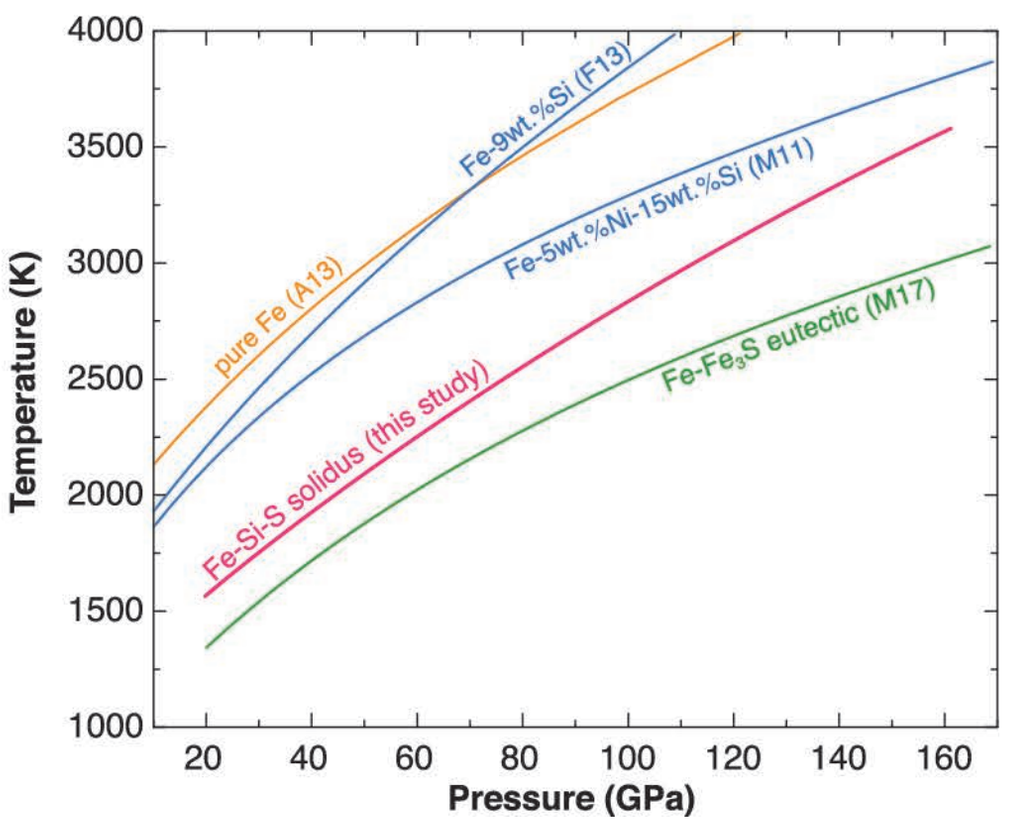

Fig. 3

This is a preprint, the final version is subject to change, of the American Mineralogist (MSA)
Cite as Authors (Year) Title. American Mineralogist, in press.
DOI: https://doi.org/10.2138/am-2018-6299

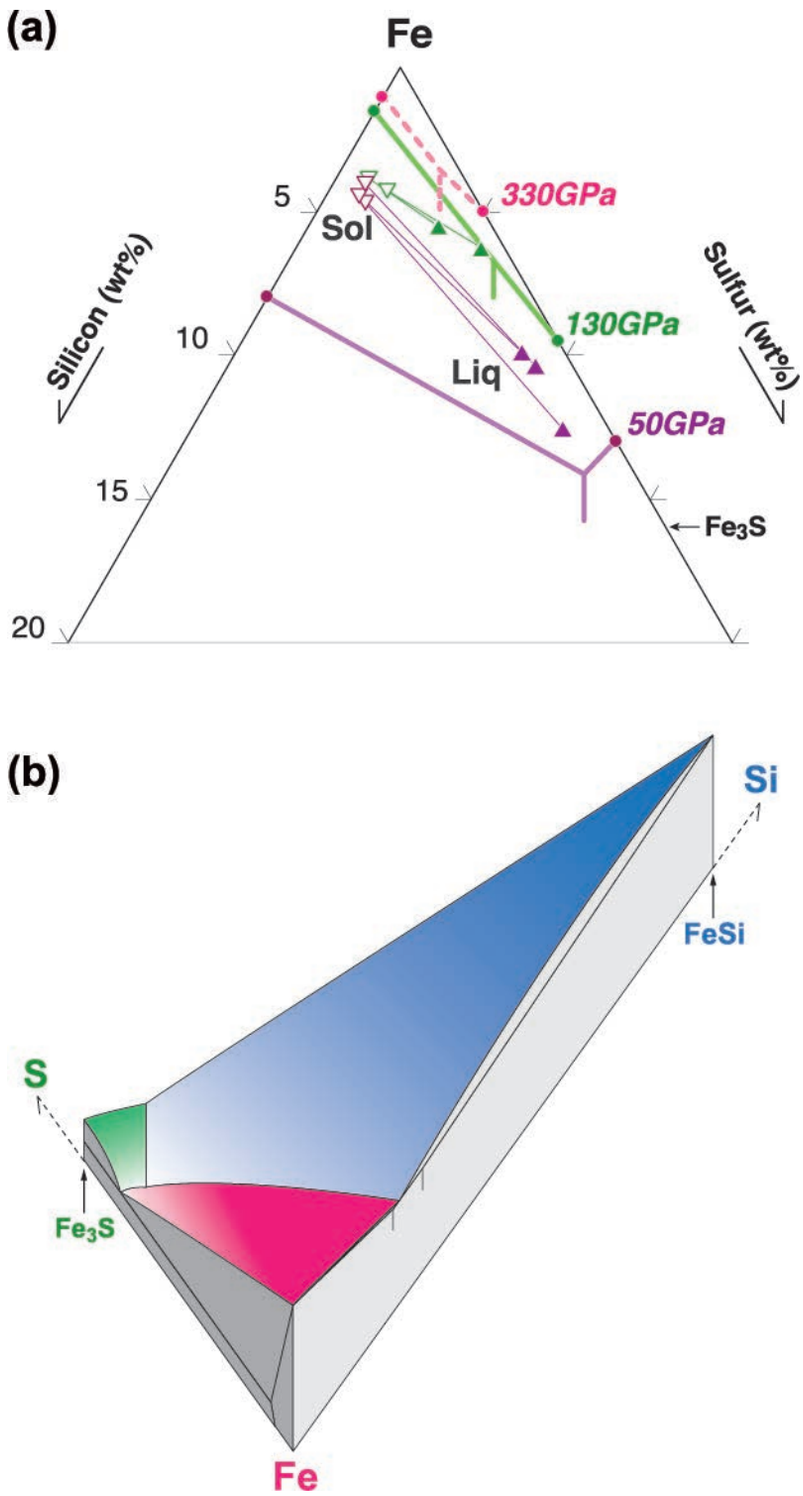

Fig. 4

This is a preprint, the final version is subject to change, of the American Mineralogist (MSA)
Cite as Authors (Year) Title. American Mineralogist, in press.
DOI: https://doi.org/10.2138/am-2018-6299

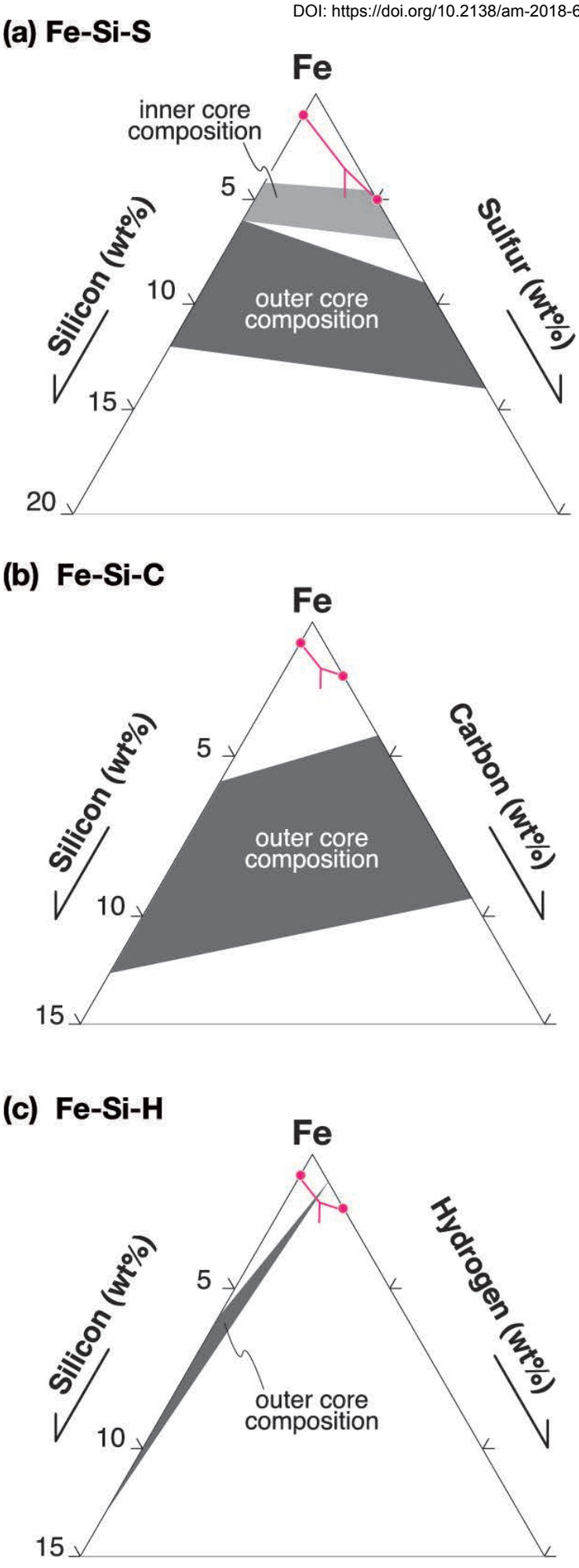

Fig. 5